# High-Contrast Material Identification by Energetic Multiparticle Spectroscopic Transmission Radiography

J. Nattress,<sup>1,\*,†</sup> T. Nolan,<sup>1</sup> S. McGuinness,<sup>2</sup> P. Rose,<sup>3,†</sup> A. Erickson,<sup>3</sup> G. Peaslee,<sup>2</sup> and I. Jovanovic<sup>1</sup>

Department of Nuclear Engineering and Radiological Sciences, University of Michigan, Ann Arbor,

Michigan 48109, USA

<sup>2</sup> Department of Physics, University of Notre Dame, Notre Dame, Indiana 46556, USA

<sup>3</sup> Nuclear and Radiological Engineering Program, G.W. Woodruff School of Mechanical Engineering, Georgia Institute of Technology, Atlanta, Georgia 30332, USA

(Received 25 January 2019; revised manuscript received 1 April 2019; published 26 April 2019; corrected 13 May 2019)

Transmission radiography using megaelectronvolt radiation is a powerful nondestructive method for determining elemental composition. Radiography is typically performed with either neutrons or photons, but neither of these probes is universally applicable. We experimentally demonstrate that a significant increase in the contrast for small elemental variations in object composition can be realized by combining the multiple-monoenergetic-neutron and multiple-monoenergetic-photon transmission radiography techniques. The multimodal source is based on deuteron-driven low-energy nuclear reactions that produce both neutrons and photons at discrete energies. The neutron time-of-flight technique is used to measure the transmission over a broad range of neutron energies and is combined with spectroscopic photon transmission radiography. This work demonstrates the use of a single, multiparticle, multiple-monoenergeticradiation source and a single type of radiation detector to simultaneously perform neutron and photon spectroscopic radiography. Four different material-identification metrics are used, which show a factor-of-3or-greater increase in sensitivity to changes in material composition when compared with traditional dualenergy photon radiography, and are in agreement with simulations that establish a direct correspondence to known photon and neutron interaction cross sections. Furthermore, the ability to infer the presence of objects consisting of impure elements, layers of different elements, or non-natural isotope concentrations is demonstrated.

DOI: 10.1103/PhysRevApplied.11.044085

### I. INTRODUCTION

Radiography is a powerful imaging technique that has found widespread use in fields such as medicine, security, and inspection of industrial processes. One of the primary objectives of radiography is to determine the geometric shape of an object or an arrangement of objects and to infer the thickness via the observed opacity. The geometric configuration alone often does not provide adequate information for the desired application [1,2]. Such is the case, for example, in screening for illicit transport of nuclear materials or narcotics, where benign substances must be distinguished from genuine threats. In the case of identification of nuclear material, the ability to differentiate among high-atomic-number (*Z*) materials could reduce scanning times for ocean-going cargo containers, an existing gap in the current U.S. nuclear-detection architecture [3].

Dual-energy photon transmission radiography is a traditional nondestructive technique that can be used to increase the contrast in radiographic images and/or determine the concentration of a particular element [4]. Since the 1950s, dual-energy (or dichromatic) transmission radiography has been used in a wide range of applications, such as improving the quality of mammograms, inspecting industrial products, and finding narcotics, explosives, weapons, and illicit nuclear materials [5,6].

Many of the applications currently use bremsstrahlung x-ray sources, where the end-point energies of the sources can be varied. The measurements made over two overlapping energy ranges are compared in such a way to qualitatively infer the effective Z of the material the x rays traverse. However, such measurements are typically made in the integral (current) mode, which reduces the value of the spectroscopic information that is contained in an individual photon's energy. Also, the lower-energy photons (well below the end-point bremsstrahlung energy) exhibit poor penetration through dense objects and may significantly contribute to the imparted radiation dose and

<sup>\*</sup>nattressjt@ornl.gov

<sup>&</sup>lt;sup>†</sup>Present address: Oak Ridge National Laboratory, Oak Ridge, Tennessee 37830, USA

degrade the image quality [7,8]. Multiple-monoenergeticphoton sources offer an advantage over bremsstrahlung sources in that the issues that arise from beam hardening do not exist [1]. A well-characterized monochromatic photon source permits the selection of specific energies that provide the most-meaningful data for a given application. In dual-energy monoenergetic photon transmission radiography [9,10], photons of two distinct energies are used to exploit the dependence of the mass attenuation coefficient on both the photon energy and the atomic number. It is desirable for the photon energies to be adequately separated to ensure that a different photon interaction mechanism (photoelectric effect, Compton scattering, or pair production) dominates at the two energies chosen, since the cross sections of these mechanisms scale differently with atomic number and thus provide the elemental contrast.

There has been increased interest in expanding the capabilities of radiographic methods to determine an object's effective atomic number while not having knowledge of the material areal density [11]. Material identification can be enhanced by combining complementary information that can be obtained from photon and neutron transmission radiography. It would be especially convenient if the nature of the probe is such that it produces both photons and neutrons. Further reducing the complexity of the approach, one could use a single type of detector capable of performing spectroscopic measurements for multiple particle types (neutrons and photons).

Here we present a radiography technique based on the same principles as dual-energy monoenergetic photon radiography, but which can significantly improve on its performance. The technique, henceforth referred to as "multiparticle spectroscopic transmission radiography" (MPSTR), merges the information obtained from spectroscopic fast-neutron and photon transmission, where the nature of both radiation probes is multiple monoenergetic. The MPSTR probe originates from the same nuclear reaction process and can accurately identify pure materials and detect mixtures of materials. Further, this method has potential for use in identification of specific organic substances present in explosives and narcotics, or in detection of the presence of shielded special nuclear material (SNM). We demonstrate that the use of dual-mode (combined neutron and gamma-ray attenuation) transmission radiography makes it possible to measure smaller changes in the elemental composition of objects compared with single-mode (pure gamma-ray attenuation) radiography, and show that the experimental results can be well predicted by simulations that use the known photon and neutron interaction cross sections. We show that on a per-particle basis (whether for neutrons or for photons), a more-precise measurement of an unknown pure material is possible when combined neutron and gamma-ray radiography is performed as compared with single-particle (gamma-ray) radiography. Finally, we demonstrate how the multiple metrics can be used to infer anomalies that imply the presence of elemental mixtures, non-natural isotopic concentration, or objects consisting of layers of different elements.

# II. PRINCIPLES OF MULTIPARTICLE SPECTROSCOPIC TRANSMISSION RADIOGRAPHY

The neutron-gamma-ray-radiography source is based on nuclear reactions induced by few-meagaelectronvolt deuterons stopping in a boron nitride (BN) target. The induced nuclear reactions produce multiple-monoenergetic, high-energy (greater than 1 MeV) neutrons and gamma rays, which can be used to penetrate dense materials and perform spectroscopic radiography for material identification [12]. As the accelerated deuteron loses energy while stopping in the BN target, neutrons are produced at decreasing energies and are correlated to the excited states of the product nuclei and kinematics of the various reactions occurring in the target. Neutrons are continuously produced until the deuteron energy drops below the lowest of the Coulomb thresholds of target nuclei—1.7 MeV for <sup>11</sup>B. Table I lists the two main neutron-producing reactions from the deuteron-BN radiation source and the resulting gamma-ray energies [13,14].

Recently, a similar source based on deuteron stopping in natural boron was used to perform material identification by dual-energy photon transmission radiography [9,10,15]. In that work, atomic numbers and areal densities of various objects were determined by spectroscopic photon radiography using two principal gamma rays produced in the reaction. While accuracies between 5%-10% when for determination of  $Z_{\rm eff}$  were demonstrated, challenges remain when one is trying to distinguish among high-Z elements, such as distinguishing SNM (uranium and plutonium) from non-SNM (e.g., lead or tungsten) [11]. The fundamental reason for this loss of contrast is the increased relative contribution of pair production in gamma-ray interactions with high-Z materials at lower gamma-ray energies. The dominant contribution of the pair-production mechanism at the higher and lower gamma-ray energies (4.4 and 15.1 MeV) used for spectroscopic radiography makes the gamma-ray cross-section scaling with Z nearly

TABLE I. Major reactions occurring in the deuteron-BN source with associated prominent gamma-ray energies [13,14].

Reaction	Q (MeV)	Gamma-ray energies (MeV)
$\frac{11}{11}B(d,n\gamma)^{12}C$	13.73	4.44, 9.64, 15.1
$^{14}N(d,n\gamma)^{15}O$	5.07	5.18, 5.24, 6.18, 6.79, 7.28, 7.56

identical at the two energies, reducing the performance of this method for Z discrimination.

Several different photon and neutron sources have been suggested for use in a material-identification MPSTR system [6]. Previously, MPSTR was implemented by combining a small, compact D-T neutron generator with a radioisotope gamma-ray source [16]. The system was able to produce highly resolved radiographic images of airfreight containers. A MPSTR system using a D-T neutron source in combination with continuous high-energy x rays was explored, but no substantial work has used this specific combination [17,18]. Another MPSTR system used a high-energy accelerator to accelerate deuterons into a gold or an aluminum target, producing neutrons and photons [19]. In that work, a broad range of photon energies were measured with an end-point energy close to 10 MeV. Neutrons at an approximate energy of 8.5 MeV were also produced. However, no robust material identification was reported. In Ref. [20], it was suggested that MPSTR could be used to detect SNM in cargo containers. In that work, deuterons were accelerated into a boron target to produce both neutrons and photons. MPSTR was not pursued, nor was there an attempt to perform material discrimination using MPSTR. To date, no work has been reported using a single source to perform material identification using MPSTR. Furthermore, no single type of detector has been used to simultaneously measure neutron and photon spectroscopic attenuation to support the material identification by MPSTR. Lastly, no work has been conducted that combines multiple spectroscopic MPSTR signals to perform material identification.

In a simple one-dimensional case, interaction of a beam of monoenergetic photons with an absorber may be described as

$$I = I_0 \exp(-\mu_t x), \tag{1}$$

where I and  $I_0$  are the intensities of the transmitted photons that did not undergo interactions with and without the absorber present, respectively,  $\mu_t$  is the total linear attenuation coefficient, and x is the absorber thickness. Interaction of a beam of monoenergetic neutrons with an absorber may be described similarly to that for photons:

$$I = I_0 \exp(-\Sigma_t x), \tag{2}$$

where  $\Sigma_t$  is the total neutron macroscopic cross section of the absorber, and I and  $I_0$  are the intensities of the noninteracting neutrons with and without the absorber present, respectively. A nonparaxial geometry, which can result from a short source-to-object or object-to-detector distance, can limit the validity of the simple one-dimensional attenuation model. In such cases, scattering can contribute significantly to the detected radiation flux. While the scattering can be adequately modeled and accounted for, accurate estimation of the magnitude of this correction requires

*a priori* knowledge of the composition and geometry of the scattering object. The following simplified analysis is therefore limited to the near-paraxial case.

Using the unique dependence of neutron interaction properties that depend on both the atomic number and the nucleon number, a quantity R indicating the material type can be defined that is directly correlated to energy-dependent neutron and photon cross sections. Similarly to dual-energy photon radiography, taking the ratio of  $\mu_t$  in Eq. (1) and  $\Sigma_t$  in Eq. (2) eliminates the dependence of R on material mass and thickness:

$$R = \frac{\mu_t}{\Sigma_t} = \frac{\ln(I_{E_\gamma}/I_{E_\gamma,0})}{\ln(I_{E_n}/I_{E_n,0})} = \frac{\ln T_{\gamma,E_1}}{\ln T_{n,E_2}}.$$
 (3)

With use of Eq. (3), *R* values corresponding to attenuation of monoenergetic photons and neutrons of given energies can be established. These *R* values can then be experimentally determined by measuring the attenuation of two particle types at given energies. In the case of commonly used bremsstrahlung radiation with changing end points, the aforementioned ratio may become sensitive to areal density [21]. In this case, the ratio is no longer unique and is treated as the ratio of effective attenuation coefficients averaged over the bremsstrahlung spectra. The mass thickness is estimated from one of the bremsstrahlung spectra and a lookup table is used to estimate *Z* [21].

## III. MATERIALS AND METHODS

Experiments are conducted with the 10-MV FN tandem accelerator at the Institute for Structure and Nuclear Astrophysics (INSAP), University of Notre Dame. Neutrons and gamma rays produced from a 3-MeV deuteron incident on a thick BN target are measured with a 7.62-cm Eljen Technologies EJ-309 liquid-scintillation detector [22] in two experimental configurations.

The detector is coupled to a 7.62- to 5.08-cm conical acrylic light guide and mounted on a Hamamatsu photomultiplier tube (PMT; model number R6321). The PMT is powered with a CAEN DT5533N desktop high-voltage power supply. The PMT anode signals are digitized with a CAEN DT5730 14-bit, 500-MS/s digitizer and saved to data files for postprocessing. The digitizer is connected to a Linux-based computer via USB with a data transfer rate of 30 MB/s. The digitizer used the digital pulse processing for charge integration and pulse shape discrimination CAEN firmware package [23] and a ROOT-based graphical interface for data acquisition and display [24].

The objective in the first experimental configuration is to measure the neutron spectrum via the time-of-flight (TOF) technique. The detector is placed 7.3 m from the BN target, while a 1.3-m-thick concrete wall separates the target from the detector. The detector is placed on the beam axis, at a distance of approximately 1.8 m from the floor and more than 4 m from the surrounding walls.

A 3-mm-thick BN target, consisting of 95% boron nitride and 5% boron trioxide, is used to fully stop the 3-MeV deuterons. Because of the lack of a shielded neutron TOF tunnel at the INSAP facility, special considerations are made in the design of the experiment. The BN target and the neutron TOF detector are placed in different rooms to provide a sufficiently long distance (approximately 8 m) for the TOF measurement. The two rooms are separated by a 1.3-m-thick concrete wall, which collimates the neutron/gamma-ray source to an approximate beam diameter of 5 cm and reduces the abundance of roomscattered neutrons. The accelerator is operated to deliver a deuteron pulse every 600 ns (one-in-six pulse selection from the primary 10 MHz pulsed beam) with a current of approximately 17 nA on target. A beam buncher and sweeper reduce the duration of the deuteron pulse to less than 2 ns. Each accelerator pulse establishes a start signal,  $t_{\text{start}}$ , to mark the time the deuteron strikes the BN target. The particle detector is fixed at a measured distance, d, from the BN target. For each registered pulse in the detector, the threshold trigger time gives the time of detection,  $t_{\text{stop}}$ . The difference between  $t_{\text{start}}$  and  $t_{\text{stop}}$ , or the TOF, is tabulated.

The waveform data are processed to determine and subtract the waveform baseline and subsequently determine the pulse height, pulse-peak position, and the pulse-shape parameter (*PSP*), which allows the photon and neutron interactions to be identified. *PSP* for an event is defined by charge integration:

$$PSP = Q_{\text{tail}}/Q_{\text{full}},\tag{4}$$

where the total pulse area,  $Q_{\rm full}$ , is calculated by our integrating the waveform starting from 16 ns before the pulse peak for 200 ns, while  $Q_{\rm tail}$  is calculated by our integrating the waveform from 22 ns after the pulse-peak position to the end of the full integration bound.

Figure 1 shows the recorded event pulse shape and light-output characteristics. The neutron and photon events are selected with a simple fiducial cut, where the events

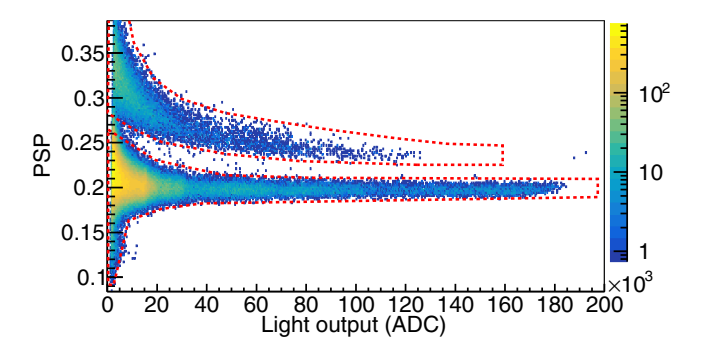


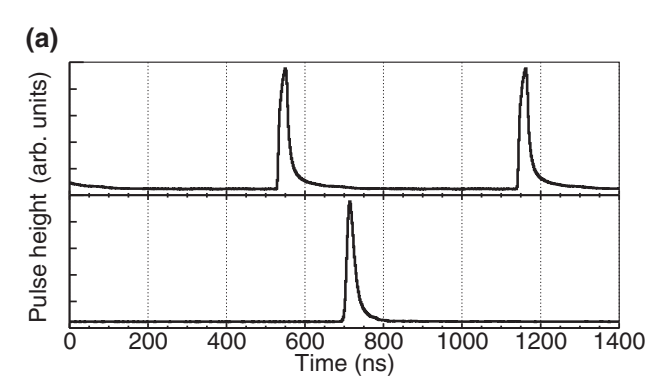
FIG. 1. Event characteristics recorded by the liquidscintillation detector with neutron and photon event selections shown (dotted red line). ADC, analog-to-digital conversion.

within the cut with PSP > 0.22 are categorized as neutron interactions, while events within the lower cut centered at approximately  $0.2\ PSP$  are categorized as photon interactions.

The selected photons are used to determine the time when a deuteron strikes the BN target, which results in prompt gamma-ray emission. Figure 2 shows example recorded photon and neutron pulses and the corresponding accelerator pulses recorded during data acquisition. These prompt photons are produced by the deuteron striking the BN target and can be used to determine the time when the deuteron strikes the target relative to the accelerator signal. With this time correlation, the neutron TOF can be calculated. The width of the prompt-gamma-ray peak is 5.85 ns, which results in a neutron energy resolution of approximately 1 MeV at 14.5 MeV and approximately 20 keV at 4 MeV. The TOF data for the selected neutron events are subsequently used to calculate the neutron energy spectrum.

The resulting spectrum is shown in Fig. 3, and is in good agreement with spectra measured in similar experiments with the  $^{11}$ B(d,n $\gamma$ ) $^{12}$ C reaction [12,20]. A significant broadening of the discrete neutron energy spectrum is observed, which is caused by the extended energy range of deuterons during their stopping in the thick BN target.

Five metallic test objects consisting of a single element (Al, Cu, Sn, Pb, and Bi) and one tungsten-alloy test object



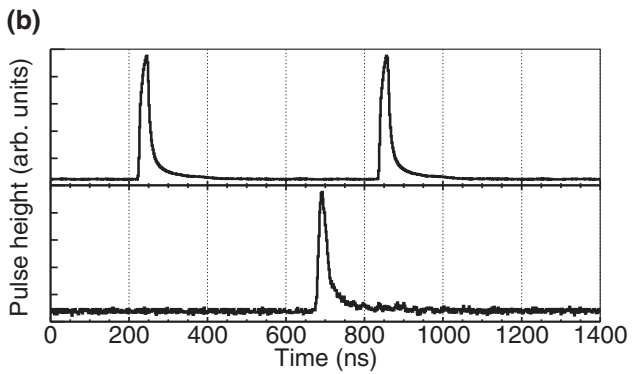


FIG. 2. (a) Accelerator signal (top) and corresponding photon event (bottom) and (b) accelerator signal (top) and corresponding neutron event (bottom) recorded during data acquisition.

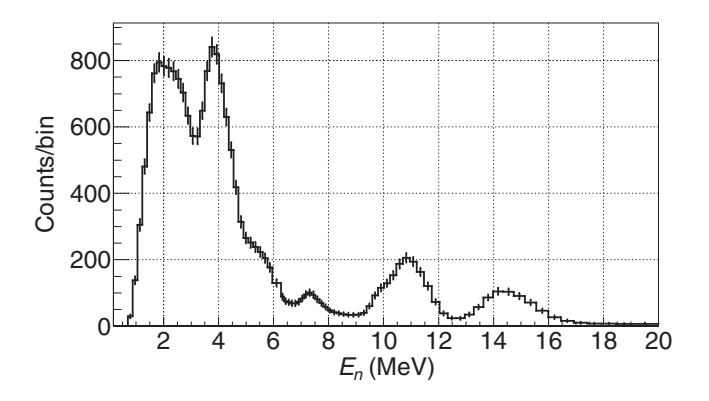


FIG. 3. Neutron energy spectrum reconstructed from the TOF measurement.

(6% Ni, 4% Cu, and 90% W) are inserted into the beam path for transmission measurements; the particle transmission is measured for 120 min per object. All test objects consist of elements in their natural isotopic abundance mix. The effective atomic number for the tungsten alloy is calculated with a custom open-source software program, Auto- $Z_{\rm eff}$  [25]. Objects are placed one at a time at a distance of 60 cm from the face of the detector. Figure 4 illustrates the neutron TOF experimental configuration with an A indicating the detector location.

Table II lists the characteristics of the objects used for the transmission measurements.

Monte Carlo simulations are performed in the GEANT4 framework [26] with the principal neutron energies produced (Fig. 3) in the deuteron-BN reaction (4, 7.5, 11, and 14.5 MeV). The exact dimensions and compositions of the test objects are modeled to study the effects of buildup in the detector, which correspond to particles that undergo scatter in the test object and subsequently produce a signal in the detector. For each of the objects, 10<sup>5</sup> neutrons at each of four principal neutron energies are simulated; all neutrons that have their energy reduced by scattering and

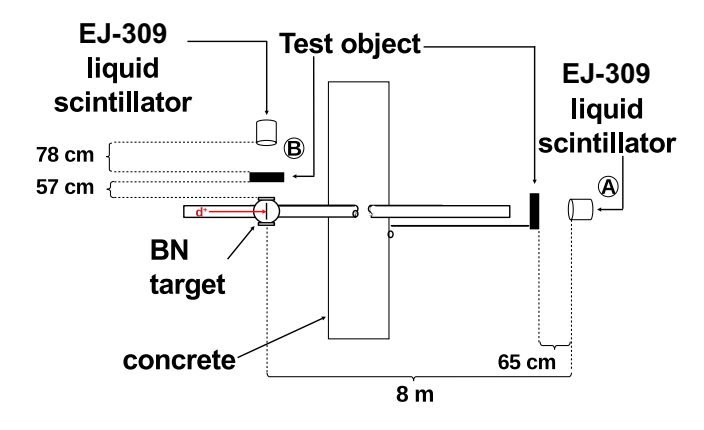


FIG. 4. Layout of the experiment: detector placement for the neutron TOF experiment (A) and for the continuous-beam photon measurements (B).

TABLE II. Properties of objects used in particle transmission experiments.

Material	Z	Density (g/cm <sup>3</sup> )	Areal density (g/cm <sup>2</sup> )
Al	13	2.7	18.1
Cu	29	8.96	17.1
Sn	50	7.3	25.1
W alloy	64.7	17	25.3
Pb	82	11.34	22.5
Bi	83	9.78	30.3

then their energy deposited in the detector are tallied. The buildup effects are found to be negligible, as less than 1% of neutrons interact with the detector.

As in the neutron TOF experiment, neutron and photon events are categorized on the basis of their pulse shape. Because of the limited availability of experimental time, the experimental configuration is altered to achieve sufficient counting statistics when we are measuring the 15.1-MeV gamma rays from the deuteron-BN source. In the second experimental configuration (marked as B in Fig. 4), the detector and test objects are moved to the same room as the BN target, which shortens the detectorto-source distance and removes the concrete collimator. The detector is placed at an angle of approximately 90° with respect to beam axis, with the face of the detector 78 cm from the BN target, and the accelerator is operated in continuous mode for this measurement with a current of approximately 160 nA on the target. The objects are inserted between the BN target and the detector, and the particle transmission is measured for 30 min per object. The objects are placed so that they subtend the entire solid angle of the detector.

Figure 5 shows the measured light-output photon spectrum, with a distinct region due to 15-MeV-gamma-ray interactions displayed in the inset. Other features are observable in the spectrum from other prominent gamma

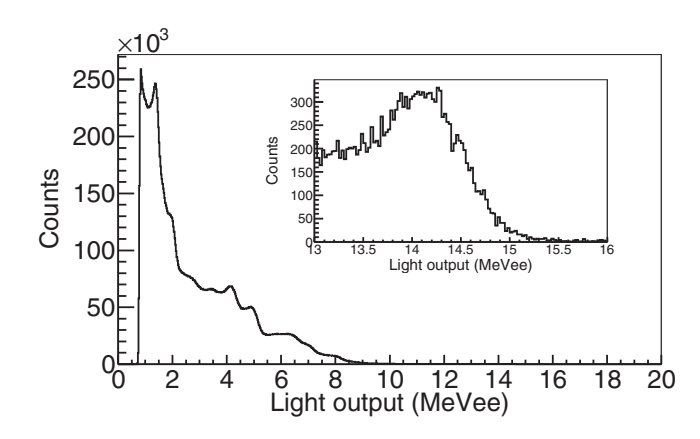


FIG. 5. Recorded unattenuated photon spectrum measured by the liquid scintillator.

rays emitted by the source, but are more difficult to identify due to the modest detector energy resolution.

Simulation models for 15.1-MeV-gamma-ray interaction with the liquid scintillator were previously developed and benchmarked with the measured light-output spectra. The model is based on the GEANT4 toolkit and useses the standard electromagnetic physics package [26]. The detector resolution is characterized by the procedure outlined in Ref. [27].

A separate scintillation detector is used to monitor any accelerator beam-current fluctuations and normalize the individual object transmission measurements. The detector is located approximately 4 m from the BN target. Photon events located in the high edge of the light-output distribution (10-15 MeVee) are selected, and the average detected photon rate is calculated. A normalization factor is calculated by our dividing the measured photon rates observed during each of the object experiments by the photon rate observed during the unattenuated-source measurement. The calculation of the neutron and photon transmission uses the unattenuated number of counts at each energy measured with the TOF detector increased by its corresponding normalization factor. This procedure is followed for the both pulsed-beam experiment and the continuous-beam experiment, with the continuous-beam experiment yielding similar results.

Because of the smaller target-to-object and object-todetector distances in the continuous-beam experiment, gamma rays that undergo scattering could contribute significantly to the recorded events in the detector. To fully understand the simulated detector response to 15.1-MeV gamma rays, a GEANT4 simulation is performed to study the buildup originating from 15.1-MeV-gamma-ray interactions, while accounting for the dimensions and placement of each of the test objects. The simulation shows that a significant fraction of 15.1-MeV gamma rays undergo interactions that do not remove them or their secondary particle from the beam path. These scattered or secondary photons may interact with the detector and be detected, leading to departure from the simple one-dimensional Beer-Lambert attenuation model. Most scattered photons have energies well below 15.1 MeV and thus can contribute to the low end of the light-output spectrum in the detector. The fraction of photons that undergo a reaction in the object but are still detected is approximately 10% for all objects used in the experiment. The gamma-ray transmission is corrected for small-angle scatter by our scaling the total number of recorded 15.1-MeV events by the calculated buildup.

### IV. RESULTS AND DISCUSSION

The transmission of 15.1-MeV gamma rays through the test objects is experimentally measured. The contribution of the 15.1-MeV gamma rays to the detector light-output spectrum is determined in several steps. First, the measured background is subtracted from the light-output distribution. Following the subtraction, the upper range of the distribution is solely the result of interactions of the highest-energy gamma rays produced by the source, the energy of which is 15.1 MeV. Next, the simulated detector response to 15.1-MeV gamma rays is fit to the background-subtracted experimental light-output spectrum. The total number of counts in the 15.1-MeV-photon simulated-fit light-output distribution is the total number of 15.1-MeV photons detected.

Four prominent energies (4, 7.3, 11, and 14.5 MeV) are identified in the neutron energy spectrum. The neutron transmission at each of the four energies is measured by our considering the counts under the peak and the neighboring energy bins (3.97–4.11 MeV, 7.18–7.45 MeV, 10.59–11.1 MeV, and 14.2–14.9 MeV).

With use of Eq. (3), four R values can be established, corresponding to the ratio of attenuation of neutrons at four different energies and 15.1-MeV gamma rays. The calculation of the predicted R value assumes a natural isotopic abundance for materials that form the test objects. Figure 6 shows the experimentally measured R values and their comparison with the calculated R values for all naturally occurring elements.

From a measured R value, the atomic number corresponding to the natural isotopic composition of an object can be calculated. Each of the calculated R values is assumed to be normally (Gaussian) distributed, where the mean and the standard deviation of each of the distributions is equal to the measured R value and its respective standard deviation. Take, for example, the measured  $R_1$  for the Al object. The Gaussian distribution for this R would have values of 0.362 and 0.08 for the mean and the standard deviation, respectively. The calculated R values are not continuous functions but are a series of discrete points.

To determine Z and its associated uncertainty from the discrete analytical R values, Monte Carlo sampling is used. A value is randomly sampled from the normal distribution of a single R. From the sampled value, the R value is selected from the discrete analytical points in the distribution by our selecting the value with the lowest residual. This Z value is used to form a histogram.

The sampling is performed N times ( $N=10^7$ ). From the newly sampled normal distribution in Z, the mean and the uncertainty can be calculated. This Monte Carlo sampling is conducted for each of the four R values and for each of the objects. A summary of the Z estimation for each of the R values for all materials is provided in Table III; across all R values, agreement with the true Z is within  $3\sigma$  of the expected value.

Single-mode gamma-ray radiography can also be performed with the deuteron-BN source [9,10,15], which produces two prominent gamma-ray energies: 4.4 and 15.1 MeV. Interactions at these photon energies are dominated

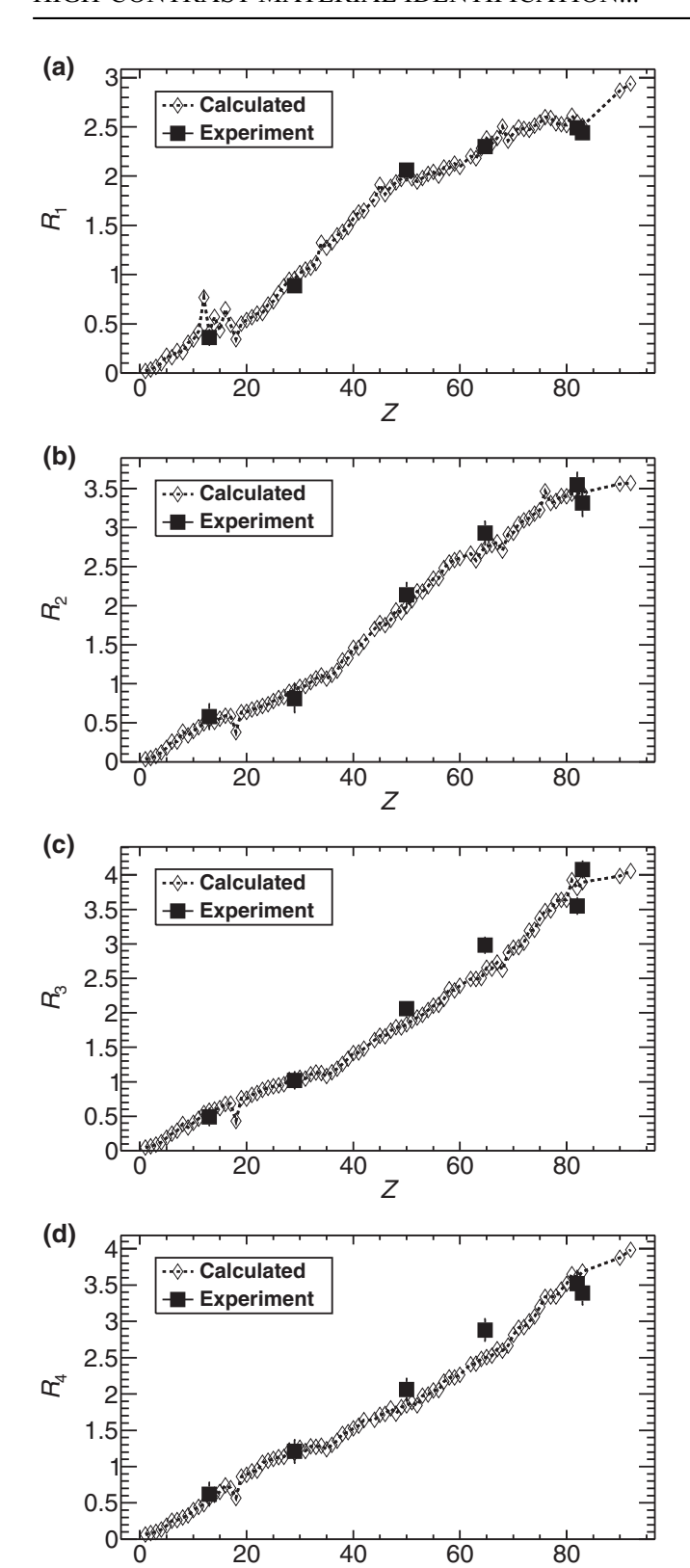


FIG. 6. The ratio of the natural log of the measured transmission of 15.1-MeV photons to (a) 4-MeV neutrons ( $R_1$ ), (b) 7-MeV neutrons ( $R_2$ ), (c) 11-MeV neutrons ( $R_3$ ), and (d) 14-MeV neutrons ( $R_4$ ) versus the ratio of the mass attenuation coefficient to the macroscopic cross section at those energies as a function of the element corresponding to Z.

Z

TABLE III. Estimation of the element, denoted with its atomic number, for each  $R_{n,y}$ .

Material	True Z	$Z(R_1)$	$Z(R_2)$	$Z(R_3)$	$Z(R_4)$
Al	13	$12.8 \pm 4.0$	$17.4 \pm 5.8$	$11.9 \pm 3.2$	$14.7 \pm 3.2$
Cu	29	$27.3 \pm 1.2$	$26.8 \pm 4.5$	$28.6 \pm 2.9$	$30.1\pm6.0$
Sn	50	$53.7 \pm 3.2$	$52.3 \pm 2.4$	$54.0 \pm 1.7$	$55.8 \pm 3.0$
W alloy	64.7	$63.6 \pm 2.4$	$67.4 \pm 3.7$	$69.6 \pm 1.9$	$70.0 \pm 2.2$
Pb	82	$77.4 \pm 4.5$	$78.6 \pm 2.7$	$77.3 \pm 4.9$	$81.4 \pm 1.8$
Bi	83	$71.1 \pm 4.7$	$77.9 \pm 5.7$	$90.1 \pm 3.6$	$79.3 \pm 3.0$

by different mechanisms, which scale differently with atomic number. At 4.4 MeV, the dominant interaction process is Compton scattering (proportional to Z), whereas pair production (proportional to  $Z^2$ ) is the dominant process for most elements at 15.1 MeV.

Figure 7 shows the energy-dependent variation of the total attenuation coefficient for uranium, lead, iron, and aluminum, which represent low-Z (Al), mid-Z (Fe), and high-Z (Pb and U) materials. The attenuation coefficients at 15.1 MeV are greater than those at 4.4 MeV for the mid- and high-Z materials. These differences in attenuation allow the separation of high-Z elements from low- and mid-Z elements, but typically do not provide sufficient contrast to distinguish among high-Z elements.

For transmission measured at two distinct energies ( $E_1$  and  $E_2$ ), one can write

$$R = \frac{\mu_1}{\mu_2} = \frac{\ln T_{E_1}}{\ln T_{E_2}},\tag{5}$$

where R is the ratio of the mass attenuation coefficients (or attenuation coefficients) at energies  $E_1$  and  $E_2$ , which is unique to the element the photons traverse. Therefore, the ratio of the mass attenuation coefficients at two energies can be compared with the experimentally measured quantity  $\ln T_{E_1} / \ln T_{E_2}$ . If the analytically calculated ratio  $(R_{\gamma})$  of attenuation of monoenergetic photons of 15.1 and 4.4

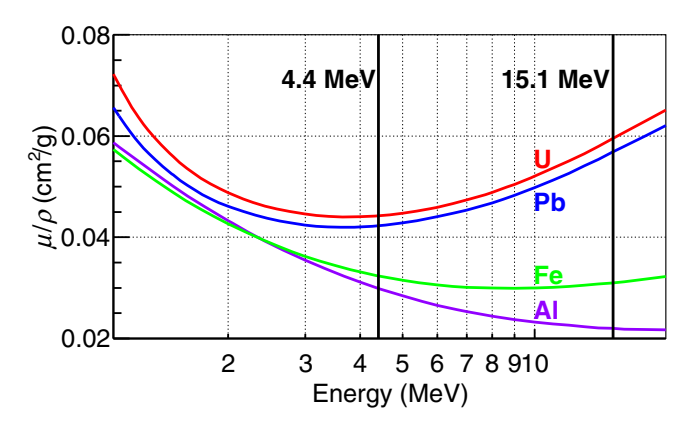


FIG. 7. Energy-dependent variation of the total attenuation coefficient for uranium (red), lead (blue), iron (green), and aluminum (purple) with two gamma-ray energies used for dual-energy transmission radiography [28].

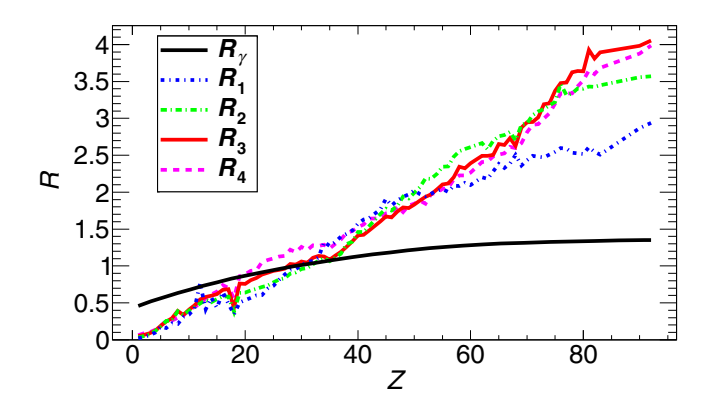


FIG. 8. Single-mode and dual-mode R values.

MeV is used as an example single-mode metric, the material discriminating power can be compared between single-and dual-particle metrics.

Figure 8 shows the calculated single-mode and dualmode material-determination R values for all naturally occurring elements in the periodic table. The improved material-discrimination capability of the  $R_{n,\gamma}$  values when compared with the pure gamma-ray metric,  $R_{\gamma}$ , is qualitatively evident in Fig. 8. The variation between a range of elements can be described by the rate of change (the slope) of a line between two points. In our case, the greater the rate of change, the better the ability of the particular attenuation factor to distinguish between elements. The rate of change of the single-mode discriminant (attenuation of monoenergetic photons of 15.1 and 4.4 MeV) is a factor of 3 or greater lower than that of all combined neutron-photon attenuation R values. The power of the combined neutron-photon attenuation factors is further evident among high-Z elements ( $74 \le Z \le 92$ ), where the  $R_{n,\gamma}$  values show an order-of-magnitude-greater rate of change with Z compared with the pure gamma-ray metric,  $R_{\nu}$ . The level of material discrimination in the high-Z range could enable discrimination between Pb and U, which would prove useful for many nuclear-security and nonproliferation applications.

For practical applications such as cargo or luggage screening, often the object or objects being measured do not consist of a single element but are a mixture of different elements and thicknesses. For objects consisting of a single element with natural isotopic abundance, all experimentally measured R values would be reconstructed to the same atomic number Z. A deviation from consistency of this reconstruction would indicate that the object does not consist of a single element in natural isotopic concentration, or that multiple layers of different elements are present in the beam path. Figure 9 presents the analytically calculated R values and their corresponding Z values for two shielded-object scenarios: uranium shielded with 10 cm of low-density polyethylene and uranium shielded with 10 cm of iron. The R values indeed cannot be reconstructed

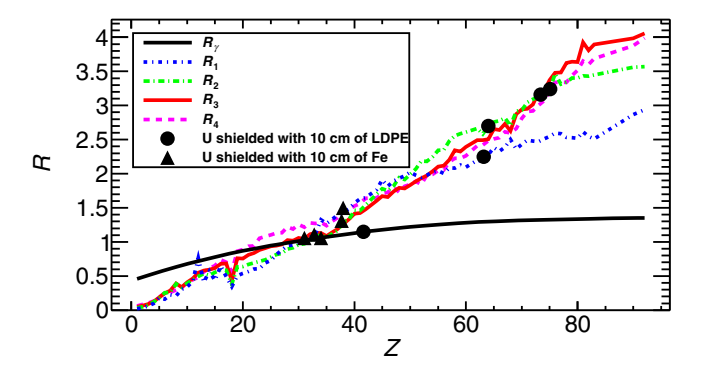


FIG. 9. Single-mode and dual-mode *R* values and the *R* values calculated for two shielded scenarios: (i) 1.1 cm of uranium shielded with 10 cm of low-density polyethylene (LDPE) and (ii) 1.1 cm of uranium shielded with 10 cm of iron.

to identical Z values for either of the shielded uranium objects. This inconsistency in Z reconstruction for various R values therefore successfully provides an indication that the object does not consist of a single element in natural isotopic concentration, but is rather a mixture or multiple elements, includes non-natural isotope concentrations, or may be composed of multiple layers of different elements.

This result could aid in anomaly detection and provide information about possible shielding or a mixture of materials in the beam's path. By use of multiple metrics (multiple *R* values), these combinations of materials and shielding are readily discernible. As a natural extension of this method, it is possible to hypothesize on the composition of materials and thicknesses of shielded objects and check for their consistency with multiple material discriminating factors (*R*) to arrive at the best interpretation.

The information gained on a per-particle basis can be compared between single-mode and dual-mode R values. Monte Carlo simulations are performed in GEANT4 with the principal neutron energies (4, 7.5, 11, and 14.5 MeV) and gamma-ray energies (4.4 and 15.1 MeV) produced in the deuteron-BN reaction and the dimensions of the aluminum, tin, and lead objects, which represent a low-Z, a mid-Z, and a high-Z object, respectively. At each of the discrete neutron and photon energies, 10<sup>6</sup> particles are directed in a beam with the exact size and shape of the respective object perpendicular to the object's face. The number of particles that traverse the target unimpeded are tallied. From these results, the five different R values and their corresponding uncertainty in Z are calculated. Figure 10 shows the uncertainty in Z for each of the five Rvalues for aluminum, tin, and lead.

For each element, the dual-mode metric outperforms the single-mode metric and increases the precision of the reconstructed object's elemental composition. The optimal dual-mode metric changes as a function of Z, which should be considered when one is designing an experiment for a specific material or application. Depending on the

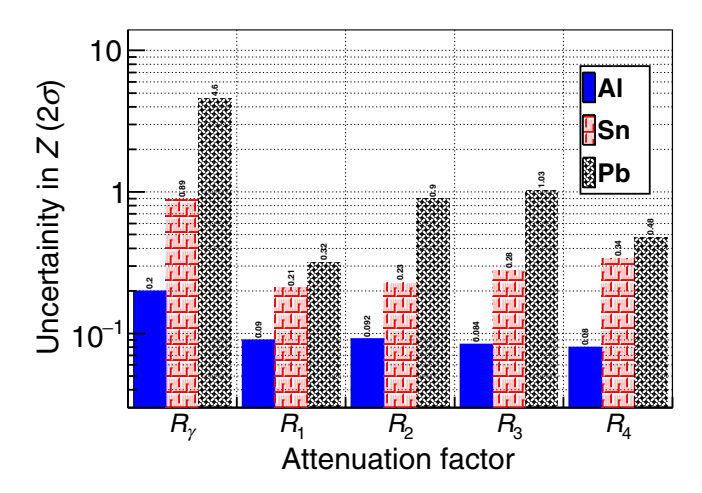


FIG. 10. Uncertainty in Z calculated from each of the five R values for aluminum, tin, and lead with a fixed number of source particles N (N=10 $^6$ ).

elemental precision required, the radiation sources and combinations of particles and energies could be specifically tailored for a given application. Although only three materials are analyzed here, the greater elemental reconstruction power of the combined neutron-photon attenuation metric over the pure photon metric is evident.

#### V. CONCLUSIONS

An alternative transmission radiography technique that combines neutron and photon transmission is explored with a deuteron-BN source. It is shown that, by use of the experimentally measured transmission of two particle types, increased sensitivity to changes in elemental composition and higher precision in elemental reconstruction is achieved as compared with a single-particle approach. Four preliminary metrics are developed on the basis of neutron and photon transmission and show promise for improved material discrimination. Reconstruction of the elemental composition for various materials using combined neutron-photon transmission radiography yielded agreement with simulations that make use of known, tabulated cross sections.

By measurement of the neutron TOF, the incident-neutron energy spectrum can be determined. If the neutron light-output distribution contains suitably distinct features, unfolding algorithms can be used to perform neutron spectroscopy without TOF measurement. The EJ-309 detector may not be the ideal detector to use for neutron-spectrum unfolding. Detectors that deliver more-prominent features in their respective light-output distributions, such as deuterated liquids or solids [29–31] or capture-based detectors [32], could result in improved neutron-spectrum deconvolution. By performing spectral unfolding to measure neutron energy, an accelerator used for this radiography technique could be operated in

continuous mode. With a duty cycle near 100% and accelerator currents on the order of milliamperes (available from next-generation compact superconducting cyclotrons), significantly shorter experimental times could be achieved to yield equivalent material-identification results.

#### ACKNOWLEDGMENTS

This work was supported by the U.S. Department of Homeland Security (Grants No. 2014-DN-077-ARI078-02 and No. 2015-DN-077-ARI096). The research of J.N. was performed under appointment to the Nuclear Nonproliferation International Safeguards Fellowship Program sponsored by the National Nuclear Security Administration's Office of International Safeguards (Grant No. NA-241).

- [1] C. Rizescu, C. Beşliu, and A. Jipa, Determination of local density and effective atomic number by the dual-energy computerized tomography method with the <sup>192</sup>Ir radioisotope, Nucl. Instrum. Methods Phys Res. Sect. A 465, 584 (2001).
- [2] V. Ryzhikov, S. Naydenov, G. Onyshchenko, P. Lecoq, and C. Smith, A spectrometric approach in radiography for detection of materials by their effective atomic number, Nucl. Instrum. Methods Phys. Res. Sect. A 603, 349 (2009).
- [3] S. Martonosi, D. Ortiz, and H. Willis, in *The Economic Impacts of Terrorist Attacks* (Routledge, London, 2007), p. 218.
- [4] B. Jacobson, Dichromatic absorption radiography. Dichromography, Acta. Radiol. 39, 437 (1953).
- [5] S. Kappadath and C. Shaw, Dual-energy digital mammography: Calibration and inverse-mapping techniques to estimate calcification thickness and glandular-tissue ratio, Med. Phys. 30, 1110 (2003).
- [6] Y. Liu, B. Sowerby, and J. Tickner, Comparison of neutron and high-energy X-ray dual-beam radiography for air cargo inspection, Appl. Radiat. Isot. **66**, 463 (2008).
- [7] C. Geddes, B. Ludewigt, J. Valentine, B. Quiter, M.-A. Descalle, G. Warren, M. Kinlaw, S. Thompson, D. Chichester, and C. Miller *et al.*, Impact of Monoenergetic Photon Sources on Nonproliferation Applications Final Report, Tech. Rep. (Idaho National Lab.(INL), Idaho Falls, ID (United States), 2017).
- [8] J. Jones, J. Sterbentz, W. Yoon, and D. Norman, in *AIP Conference Proceedings* (AIP, 2009), Vol. 1194, p. 43.
- [9] P. Rose, A. Erickson, M. Mayer, J. Nattress, and I. Jovanovic, Uncovering special nuclear materials by lowenergy nuclear reaction imaging, Sci. Rep. 6, 24388 (2016).
- [10] B. Henderson, H. Lee, T. MacDonald, R. Nelson, and A. Danagoulian, Experimental demonstration of multiple monoenergetic gamma radiography for effective atomic number identification in cargo inspection, J. Appl. Phys. 123, 164901 (2018).
- [11] S. Naydenov, V. Ryzhikov, and C. Smith, Direct reconstruction of the effective atomic number of materials by the method of multi-energy radiography, Nucl. Instrum. Methods Phys. Res. Sect. B 215, 552 (2004).

- [12] T. Taddeucci, R. Sheffield, T. Massey, D. Carter, J. O'Donnell, C. Brune, D. Ingram, D. Jacombs, and A. DiLullo, Neutron and gamma-ray production with lowenergy beams, Los Alamos National Laboratories Report LA-UR-07-2724 (2007).
- [13] J. Kelley, J. Purcell, and C. Sheu, Energy levels of light nuclei A = 12, TUNL Nuclear Data Evaluation Project (2019).
- [14] F. Ajzenberg-Selove, Energy levels of light nuclei A = 15, TUNL Nuclear Data Evaluation Project (2019).
- [15] B. O'Day III, Z. Hartwig, R. Lanza, and A. Danagoulian, Initial results from a multiple monoenergetic gamma radiography system for nuclear security, Nucl. Instrum. Methods Phys. Res. Sect. A 832, 68 (2016).
- [16] J. Eberhardt, S. Rainey, R. Stevens, B. Sowerby, and J. Tickner, Fast neutron radiography scanner for the detection of contraband in air cargo containers, Appl. Radiat. Isot. 63, 179 (2005).
- [17] K. Kang, H. Hu, Y. Xie, Q. Miao, Y. Yang, Y. Li, Z. Chen, and X. Wang, Method and equipment for discriminating materials by employing fast neutron and continuous spectral x-ray, US Patent 7,399,976 (2008).
- [18] B. Sowerby and J. Tickner, Radiographic equipment, International Patent Application No, Tech. Rep. (PCT/AU03/01641, Filing date: 10 Dec, 2003).
- [19] J. Rynes, J. Bendahan, T. Gozani, R. Loveman, J. Stevenson, and C. Bell, Gamma-ray and neutron radiography as part of a pulsed fast neutron analysis inspection system, Nucl. Instrum. Methods Phys. Res. Sect. A 422, 895 (1999).
- [20] M. Brandis, V. Dangendorf, C. Piel, D. Vartsky, B. Bromberger, D. Bar, E. Friedman, I. Mardor, I. Mor, and K. Tittelmeier *et al.*, in *AIP Conference Proceedings* (AIP, 2011), Vol. 1336, p. 711.
- [21] S. Ogorodnikov and V. Petrunin, Processing of interlaced images in 4–10 MeV dual energy customs system for material recognition, Phys. Rev. Spec. Top. Accel Beams 5, 104701 (2002).
- [22] Eljen Technologies, Neutron/Gamma PSD Liquid Scintillator Data Sheet EJ-301, EJ-309, (Date Accessed: Apr 22, 2017).
- [23] DPP PSD User Manual UM2580, (2015), User's Manual for the DT 5730.

- [24] Z. Hartwig, The ADAQ framework: An integrated toolkit for data acquisition and analysis with real and simulated radiation detectors, Nucl. Instrum. Methods Phys. Res. Sect. A 815, 42 (2016).
- [25] M. Taylor, R. Smith, F. Dossing, and R. Franich, Robust calculation of effective atomic numbers: The Auto-Z<sub>eff</sub> software, Med. Phys. 39, 1769 (2012).
- [26] S. Agostinelli, J. Allison, K. A. Amako, J. Apostolakis, H. Araujo, P. Arce, M. Asai, D. Axen, S. Banerjee, and G. Barrand *et al.*, Geant4–a simulation toolkit, Nucl. Instrum. Methods Phys. Res. Sect. A 506, 250 (2003).
- [27] J. Nattress and I. Jovanovic, Response and calibration of organic scintillators for gamma-ray spectroscopy up to 15-MeV range, Nucl. Instrum. Methods Phys. Res. Sect. A 871, 1 (2017).
- [28] M. Berger and J. Hubbell, XCOM: Photon cross sections on a personal computer, Tech. Rep. (National Bureau of Standards, Washington, DC (USA). Center for Radiation, 1987).
- [29] F. Becchetti, R. Raymond, R. Torres-Isea, A. Di Fulvio, S. Clarke, S. Pozzi, and M. Febbraro, Recent developments in deuterated scintillators for neutron measurements at low-energy accelerators, Nucl. Instrum. Methods Phys. Res. Sect. A 874, 72 (2017).
- [30] M. Carman, A. Glenn, A. Mabe, F. Becchetti, S. Payne, and N. Zaitseva, Solution growth of a deuterated trans-stilbene crystal for fast neutron detection, J. Cryst. Growth 498, 51 (2018).
- [31] F. Becchetti, R. Torres-Isea, A. Di Fulvio, S. Pozzi, J. Nattress, I. Jovanovic, M. Febbraro, N. Zaitseva, and L. Carman, Deuterated stilbene (stilbene-d12): An improved detector for fast neutrons, Nucl. Instrum. Methods Phys. Res. Sect. A 908, 376 (2018).
- [32] J. Nattress, M. Mayer, A. Foster, A. B. Meddeb, C. Trivelpiece, Z. Ounaies, and I. Jovanovic, Capture-gated spectroscopic measurements of monoenergetic neutrons with a composite scintillation detector, IEEE Trans. Nucl. Sci. 63, 1227 (2016).

Correction: The affiliation address of the third author contained a production error and has been fixed.